

Application of fluence field modulation to proton computed tomography for proton therapy imaging

G Dedes¹, L De Angelis¹, S Rit², D Hansen³, C Belka⁴,
V Bashkirov⁵, R P Johnson⁶, G Coutrakon⁷, K E Schubert⁸,
R W Schulte⁵, K Parodi¹ and G Landry¹

¹ Faculty of Physics, Department of Medical Physics, Ludwig-Maximilians-Universität München (LMU Munich), 85748 Garching, Germany

² Univ Lyon, INSA—Lyon, Université Claude Bernard Lyon 1, UJM-Saint Etienne, CNRS, Inserm, CREATIS UMR 5220, U1206, F-69373, Lyon, France

³ Department of Oncology, Aarhus University Hospital, 8000 Aarhus, Denmark

⁴ Department of Radiation Oncology, LMU Munich, 81377 Munich, Germany

⁵ Division of Radiation Research, Loma Linda University, Loma Linda, CA 92354, United States of America

⁶ Department of Physics, U.C. Santa Cruz, Santa Cruz, CA 95064, United States of America

⁷ Department of Physics, Northern Illinois University, DeKalb, IL 60115, United States of America

⁸ School of Engineering and Computer Science, Baylor University, Waco, TX 76798, United States of America

E-mail: g.dedes@lmu.de

Received 3 November 2016, revised 12 May 2017

Accepted for publication 5 June 2017

Published 12 July 2017



CrossMark

Abstract

This simulation study presents the application of fluence field modulated computed tomography, initially developed for x-ray CT, to proton computed tomography (pCT). By using pencil beam (PB) scanning, fluence modulated pCT (FMpCT) may achieve variable image quality in a pCT image and imaging dose reduction.

Three virtual phantoms, a uniform cylinder and two patients, were studied using Monte Carlo simulations of an ideal list-mode pCT scanner. Regions of interest (ROI) were selected for high image quality and only PBs intercepting them preserved full fluence (FF). Image quality was investigated in terms of accuracy (mean) and noise (standard deviation) of the reconstructed proton relative stopping power compared to reference values. Dose calculation accuracy on FMpCT images was evaluated in terms of dose volume histograms (DVH), range difference (RD) for beam-eye-view (BEV) dose profiles and

gamma evaluation. Pseudo FMpCT scans were created from broad beam experimental data acquired with a list-mode pCT prototype.

FMpCT noise in ROIs was equivalent to FF images and accuracy better than -1.3% (-0.7%) by using 1% of FF for the cylinder (patients). Integral imaging dose reduction of 37% and 56% was achieved for the two patients for that level of modulation. Corresponding DVHs from proton dose calculation on FMpCT images agreed to those from reference images and 96% of BEV profiles had RD below 2 mm, compared to only 1% for uniform 1% of FF. Gamma pass rates (2%, 2 mm) were 98% for FMpCT while for uniform 1% of FF they were as low as 59%. Applying FMpCT to preliminary experimental data showed that low noise levels and accuracy could be preserved in a ROI, down to 30% modulation.

We have shown, using both virtual and experimental pCT scans, that FMpCT is potentially feasible and may allow a means of imaging dose reduction for a pCT scanner operating in PB scanning mode. This may be of particular importance to proton therapy given the low integral dose found outside the target.

Keywords: proton CT, proton therapy, imaging dose, stopping power, dose reduction, fluence modulation, pencil beam scanning

 Supplementary material for this article is available [online](#)

(Some figures may appear in colour only in the online journal)

1. Introduction

Proton computed tomography (pCT), initially proposed by Cormack (1963), has recently seen considerable research interest as a means of reducing range uncertainties in proton therapy (Paganetti 2012, Yang *et al* 2012). By measuring the position and angle of each proton, as suggested by Huesman *et al* (1975), along with the energy loss behind the patient, a relative stopping power to water (RSP) map can be directly reconstructed using dedicated reconstruction algorithms (Penfold *et al* 2009, 2010, Rit *et al* 2013, Hansen *et al* 2014, 2016). Recent detector developments coupled with improved computing power have permitted the development and operation of two list-mode pCT scanner prototypes based on broad (passively scattered) proton beam delivery (Hurley *et al* 2012, Sadrozinski *et al* 2016). The RSP accuracy of pCT is expected to improve the current clinical practice, which is based on the calibration of single energy CT scans with a reported uncertainty of 3.5% (Yang *et al* 2012). Additionally, pCT has the potential to equal or outperform the accuracy achievable with dual energy CT (Hünemohr *et al* 2013, 2014, Hudobivnik *et al* 2016, Mohler *et al* 2016), according to the simulation study of Hansen *et al* (2015). Initial results from pCT prototypes operating in list-mode suggest at least comparable accuracy to DECT with experimental RSP errors currently below 1.4% for phantoms (Giacometti *et al* 2017).

Besides RSP accuracy, pCT benefits from good dose efficiency, yielding better contrast to noise ratio at equivalent dose levels when compared to x-ray CT (Schulte *et al* 2005). Early results from pCT prototypes report doses of about 1 mGy to achieve acceptable image quality (Sadrozinski *et al* 2016). This is comparable to the imaging dose used by in-room CBCT imaging, and lower than typical x-ray CT treatment planning imaging doses (at least 10 mGy and ranging up to 100 mGy, see table 7 in Murphy *et al* (2007)). A recent DECT publication

specific to proton therapy reported doses of 20 mGy (Hudobivnik *et al* 2016). This aspect of pCT suggests the technique could be used for daily low-dose in-room imaging and could compete with x-ray cone-beam CT (CBCT) image quality without the need of corrections, as needed for proton dose calculations on CBCT images (Kurz *et al* 2015, Landry *et al* 2015a, 2015b, Park *et al* 2015, Veiga *et al* 2015, 2016). In x-ray CT, several dose reduction techniques have been developed such as the use of bow-tie filters (Graham *et al* 2007a, Mail *et al* 2009) and automatic exposure control (Mulken *et al* 2005, McCollough *et al* 2006, Kalender *et al* 2008). An exciting idea consists of prescribing image quality levels prior to CT scanning using modulation of the x-ray fluence within the fan-beam (Graham *et al* 2007b, Bartolac *et al* 2011, Bartolac and Jaffray 2013, Szczykutowicz and Mistretta 2013a, 2013b). This approach is called fluence field modulated CT (FFMCT) and was recently experimentally realized using the imaging system of a TomoTherapy machine (Szczykutowicz and Mistretta 2014, Szczykutowicz *et al* 2015). The FFMCT concept is very similar to intensity modulated radiation therapy (IMRT) where the mega-voltage photon fluence is modulated with a multi-leaf collimator. The main difficulty with modulating the x-ray fluence of a conventional CT scanner is the lack of an equivalent modulation device. For this reason, experimental realization of FFMCT made use of the TomoTherapy machine's imaging system which is equipped with a 64 leaf binary collimator. Another group has achieved FFMCT by using multiple aperture devices (Stayman *et al* 2016).

Given the current rise in the number of proton therapy centers equipped with pencil beam scanning (PBS), one can imagine imitating intensity modulated proton therapy (IMPT) instead of IMRT, to create a pencil beam (PB) pCT system allowing fluence modulated pCT (FMpCT). FMpCT would rely on beam current or delivery time modulation during the acquisition of a pCT projection to achieve the desired proton fluence modulation. Using a treatment planning image as guide, an in-room FMpCT scan could thus be acquired with high image quality in the beam path and a lower image quality in regions receiving negligible therapeutic dose levels, leading to a lower integral imaging dose compared to uniform fluence scans. Such an image could be used for patient positioning, dose recalculation or even re-planning.

The objective of this study was to evaluate the feasibility of FMpCT using a PB pCT Monte Carlo simulation framework and a state-of-the-art pCT reconstruction algorithm. For a simple homogeneous virtual phantom and two patient CT-based virtual phantoms, image quality at different modulation levels was investigated, as well as proton dose calculation accuracy. Furthermore, FMpCT was simulated using a selected subset of experimental data acquired with a state-of-the-art scanner prototype for broad beam proton irradiation.

2. Materials and methods

2.1. Proton CT simulation

The simulation platform used in this study is based on Geant4 version 10.01.p02 (Agostinelli *et al* 2003) and has been used in previous studies for proton dose calculation in voxelized geometries (Schmid *et al* 2015, Landry *et al* 2015b, Hudobivnik *et al* 2016). The reference physics list QGSP_BIC_HP was used for the simulation of interaction of particles with matter. The simulation platform uses CT images which are converted to mass density and tissue composition using the approach of Schneider *et al* (2000).

Existing list-mode pCT scanner prototypes rely on two tracker modules located up- and down-stream of the scanned object. The tracker modules are made of pairs of two orthogonal silicon strip detectors allowing position and direction detection. A calorimeter, located after the second tracker module, records the residual energy loss. A more detailed description can

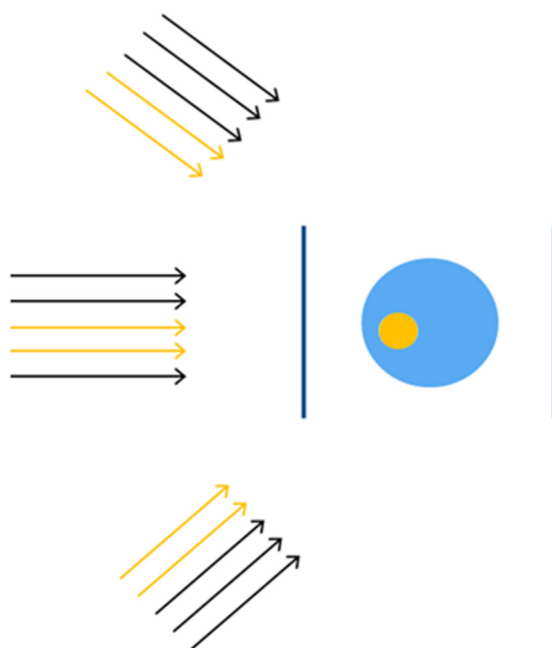


Figure 1. Schematic representation of FMpCT using PBS. PBs whose central axis geometrically intersects the ROI preserve full fluence while the others have their fluence reduced. The vertical lines represent the tracker planes for the horizontal PBs. The energy measuring detector is omitted for simplicity.

be found in Sadrozinski *et al* (2016) (see figures 1 and 2 in that publication). In this study, an ideal pCT scanner in the form of two scoring planes, before and after the scanned object (which is centered at the origin) was simulated. The two ideal scoring planes, which are of the same material as the surrounding world (air), record the exact position, direction and energy of each traversing proton. The planes are positioned perpendicularly to the X axis, which is parallel to the beam, at -15.88 cm and 15.88 cm, both covering a surface of 60×60 cm². This area was chosen for simplicity and does not represent the field of view of a real scanner. The simulated imaging beam consists of a 2D grid of non-divergent proton PBs arranged at 1 cm intervals in the YZ plane. Each PB has a 2D Gaussian proton distribution with $\sigma = 4$ mm in air. The Z extent (parallel to the superior inferior patient axis) of the PB grid was adjusted according to each virtual phantom, and the Y extent was set to 25 cm. In order to simulate a tomographic scan, the scanned phantom was rotated around the Z axis at 1° steps, covering an angular span of 360° .

2.2. Virtual phantoms

Three voxelized phantoms were used in this study. The phantoms were derived from x-ray CT scans of IMRT patients.

- (1) A simple phantom was simulated by overwriting a $1.074 \times 1.074 \times 1$ mm³ CT image with a 10 cm radius cylinder with 0 HU. Outside the cylinder -1000 HU was used. Note that when using the stoichiometric calibration, 0 HU corresponds to a predefined human tissue composition and not water. For this case a single row of PBs bisecting the cylinder was employed given the Z axis symmetry.

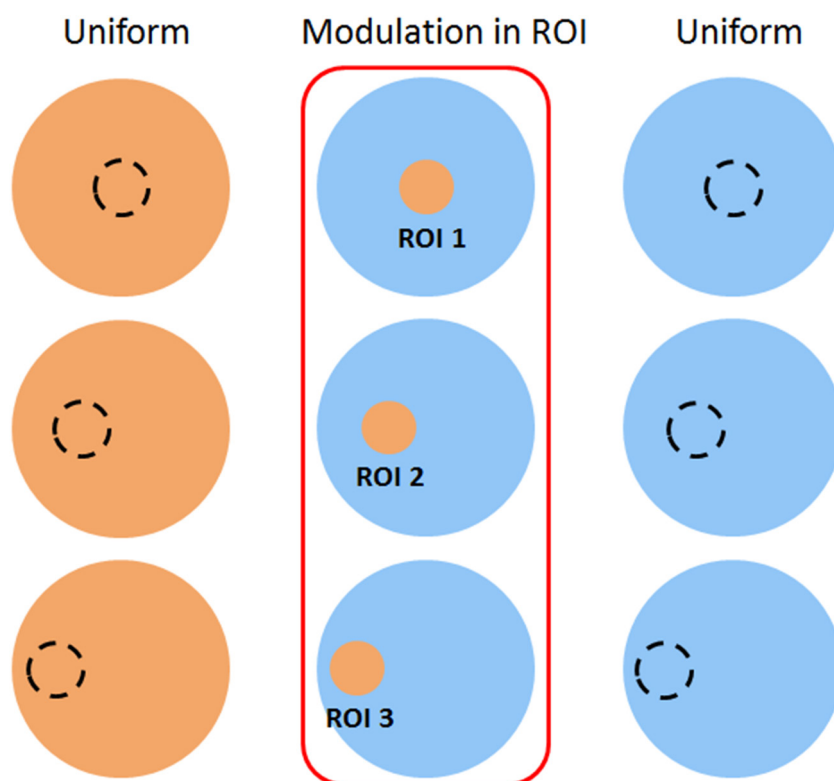


Figure 2. Homogeneous 10 cm radius phantom with three different 1 cm radius ROIs (from top to bottom). The two colors indicate high and low fluence. For each ROI, a uniform FF scan (left), a uniform scan of lower fluence FMF · FF (right), and finally three FMpCT scans of FF inside the ROI and FMF · FF outside (middle) were simulated.

- (2) The second phantom was derived from a $1.074 \times 1.074 \times 1 \text{ mm}^3$ CT scan of a patient (Pat1) treated with IMRT for a brain metastasis with a small planning target volume (PTV) located near the base of the skull. The PTV was 5 cm along the Z axis.
- (3) For the third phantom, a $1.074 \times 1.074 \times 3 \text{ mm}^3$ CT scan of a paranasal sinus cancer patient (Pat2) was used. The large PTV including lymph nodes was 14.3 cm along the Z axis. For (2) and (3), the PB grid extent in Z was set to cover the PTV plus a margin (see section 2.5).

For each phantom, a 360 projections pCT scan with 10^4 protons per PB per projection was simulated. This corresponded to $9600 \text{ protons cm}^{-2}$ in the center of a list-mode projection (protons with recorded coordinates at both the entrance and exit scoring planes, thus neglecting those having undergone nuclear interactions). For all simulations, the dose to tissue per voxel was scored.

2.3. Fluence modulation

The concept of fluence modulation based on proton PB scans presented in this work relies on the definition of regions of interest (ROIs), in which a high image quality is desirable. The term image quality here refers to RSP noise levels and RSP accuracy. The ROIs should ideally

cover the beam path including the PTV and could be derived using diagnostic or treatment planning imaging data. Phantom specific ROI generation will be presented below.

A schematic representation of the concept is shown in figure 1 for a simplified ROI. In this proof of principle study, the PB modulation pattern was obtained by calculating a binary sinogram (PB index versus projection angle). The sinogram entries were 1 if the central axis of a PB intersects the ROI in a given projection and 0 otherwise. Using this sinogram, the fluence of PBs assigned 0 is reduced by a given fluence modulation factor (FMF), $FMF < 1$, while those PBs assigned 1 preserve full fluence (FF). The modulation was performed as a post-processing step to allow several FMpCT images from a single simulation. When reducing a PB's fluence, list-mode data were randomly discarded, ensuring that the energy and spatial distribution of the PBs was preserved.

2.4. Proton CT reconstruction framework

The reconstruction algorithm chosen for this study was a filtered backprojection (FBP) implementation which accounts for the curved proton paths in the imaged object, mainly due to multiple Coulomb scattering. The main principles of the algorithm are presented in Rit *et al* (2013) and a comparison with different iterative algorithms is presented in Hansen *et al* (2016). The algorithm is based on list-mode data, and the actual path of every proton is approximated by a most likely path (MLP) formulation (Schulte *et al* 2008), which uses the position and direction information from the scoring planes.

Protons were selected with a 3 standard deviations cut on the energy and angular distributions around their mean energy and angle per projection pixel, in order to filter out nuclear reactions and large angle scattering events, whose energy loss and path cannot be described by the Bethe formula and the MLP formalism. List-mode data were binned in intermediate projection images with 1×1 mm pixels, which were then filtered and back-projected. Scans simulated with low fluences can suffer from artefacts due to the absence of proton information in some pixels of the intermediate projections. To counter this, sinogram interpolation (Hansen *et al* 2016) was used for all reconstructions. Images were reconstructed on the same grids as the CT scans used to generate the Geant4 virtual phantoms. For each phantom and each FMF, the following images were reconstructed: (1) a FF image, (2) a FMF·FF uniform fluence image and (3) a FMpCT image with a fluence of FMF·FF outside the ROI.

2.5. FMpCT ROIs and FMF

For the cylindrical phantom, simple circular ROIs with 1 cm radius were studied, as shown in figure 2. The FMF was set to 0.1, 0.05 and 0.01. ROI1 was at the center of the cylinder, ROI2 was 37.6 mm off-center and ROI3 was 75.2 mm off-center.

For Pat1 and Pat2, proton treatment plans using PBS were generated using a research version of a commercial TPS (Raystation, Raysearch Laboratories, Sweden). For Pat1, a single field uniform dose (SFUD) plan using a 220 degree gantry angle on the International Electrotechnical Commission (IEC) scale was used to deliver 60 Gy to the PTV (15 cm^3). For Pat2, a 3-field IMPT simultaneous integrated boost plan with beams at 0, 100 and 260 degrees was used. The 0 degree field was used only superiorly to the nasal cavities. The high dose PTV (174 cm^3) received 60 Gy and the lymph node PTV ($510 \text{ cm}^3 - 174 \text{ cm}^3 = 336 \text{ cm}^3$) 50 Gy. For both Pat1 and Pat2, a FMpCT ROI was obtained by using the 10 Gy isodose line, ensuring inclusion of beam paths, PTVs as well as relevant organs at risk. The ROI volumes were 220 cm^3 for Pat1 and 2021 cm^3 for Pat2, and the ROIs are shown in figure 3. For Pat1 and Pat2 FMF was set to 0.1, 0.05 and 0.01.

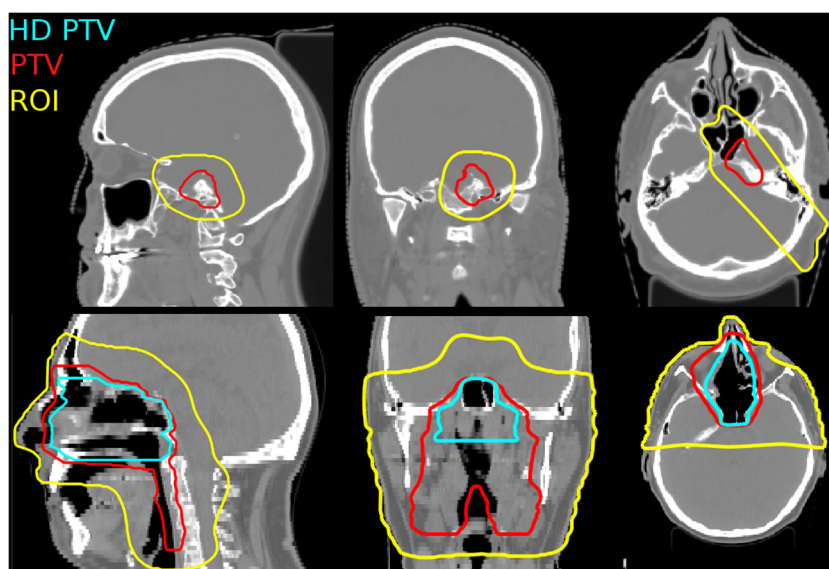


Figure 3. (top row) Axial, coronal and sagittal slices of the CT image of Pat1, including the FMpCT ROI and PTV. (bottom row) The same for Pat2, with an additional high dose PTV (HD PTV).

2.6. Image quality

The image quality was quantified according to RSP accuracy and noise. For each virtual phantom, a reference RSP distribution was obtained from Geant4 and accuracy was calculated as the mean of $(RSP - RSP_{ref})/RSP_{ref}$ in the FMpCT ROI. Noise was the standard deviation of $(RSP - RSP_{ref})/RSP_{ref}$ in the same ROI. In this study, for both noise and accuracy, relative differences of less than 0.5% (absolute value) were considered negligible. Additionally, the imaging dose reduction in the FMpCT images with respect to the FF images, as a function of FMF, was also quantified.

2.7. Dose recalculation

To evaluate dose calculation accuracy on FMpCT images, the reference 3D RSP_{ref} distributions were imported in the TPS with a custom lookup table and used to re-optimize the treatment plans of Pat1 and Pat2. Subsequently, the FF, FMF·FF and FMpCT images were also imported in the TPS and used for plan recalculation. For the SFUD beam of Pat1, beam eye view range (80% of dose maximum) differences to the RSP_{ref} image were computed for dose profiles showing maximum doses higher than 50% of the prescription dose. The percentage of profiles within 1 mm and 2 mm of the RSP_{ref} dose distribution was computed. Additionally, dose volume histograms (DVH) and 2%/2 mm gamma pass rates were obtained for the SFUD dose distribution of Pat1 and the IMPT dose distribution of Pat2. For gamma evaluation doses above 50% of the prescription dose were considered.

2.8. Experimental data

In addition to the simulated data, FMpCT was also attempted on experimental data obtained with the Phase II preclinical prototype pCT scanner (Sadrozinski *et al* 2016) of the Loma

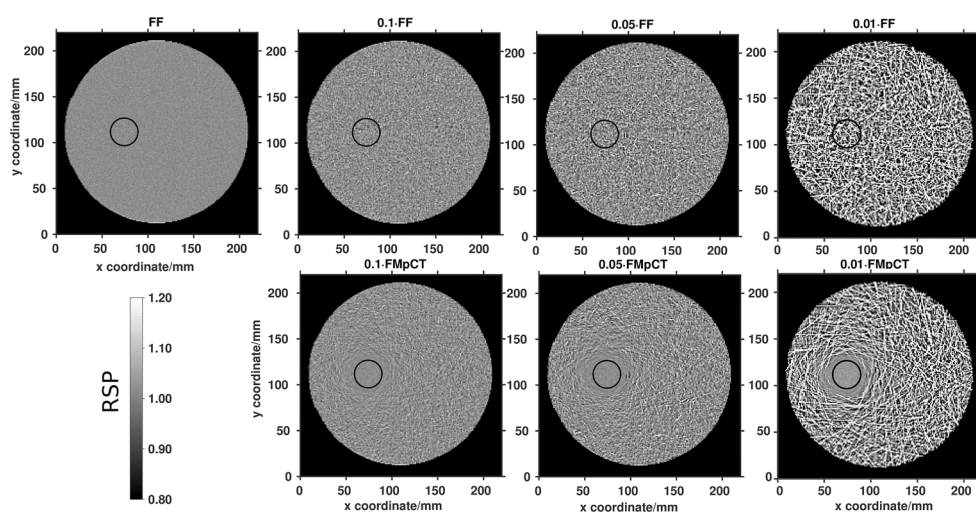


Figure 4. Upper row, left to right: FF image (10^4 protons per PB) and images obtained with homogeneous fluence of $0.1 \cdot \text{FF}$, $0.05 \cdot \text{FF}$ and $0.01 \cdot \text{FF}$. Lower row, FMpCT images corresponding to FF in each ROI (black circle) and $0.1 \cdot \text{FF}$, $0.05 \cdot \text{FF}$ and $0.01 \cdot \text{FF}$ outside. The grayscale corresponds to RSP values.

Linda University and U.C. Santa Cruz at which a pediatric head phantom (715-HN, CIRS, Norfolk, VA) was scanned. The 90 projections scan with 2.5×10^6 protons per projection was performed at the Northwestern Medicine Chicago Proton Center (NMCPC) facility, using a 200 MeV proton wobbling beam from the IBA universal nozzle for another study (Johnson *et al* 2016). The registered proton fluence per projection in the experimental data was $12\,000 \text{ cm}^{-2}$, similar to that from the simulated data. Although the actual scan was not acquired with fluence modulated PBs, fluence modulation was emulated during post-processing of the list-mode data. For every proton, a straight line path was constructed from the entrance and exit coordinates provided by the tracking system of the prototype. The protons whose straight paths did not intersect the defined ROI were removed from the data with a removal probability of 1-FMF. The goal here was to assess the impact of FMpCT on image quality compared to the FF image; the general performance of pCT for this combination of scanner and phantom has been reported elsewhere (Giacometti *et al* 2017). Thus, for this part of the study, the theoretical RSP (from Giacometti *et al* (2017)) in the homogeneous brain section of the phantom was used as reference for numerical analysis. Since no voxelized ground truth was available, the FF pCT image was used as reference in RSP voxel-by-voxel accuracy images. Given the lower number of protons in the experimental data (90 projections instead of 360), higher values of FMF = 0.5, 0.3 and 0.1 were employed. A single cylindrical ROI of 1.5 cm radius was considered (see figure 10 in the results section). The ROI was chosen to contain homogeneous phantom brain material for image quality analysis, given the absence of a voxelized reference at the time of writing.

3. Results

3.1. Uniform phantom

In figure 4, the reconstructed pCT images of the cylindrical phantom are shown. With increasing FMF, the noise in the images increases as expected. In the case of the FMpCT images, the

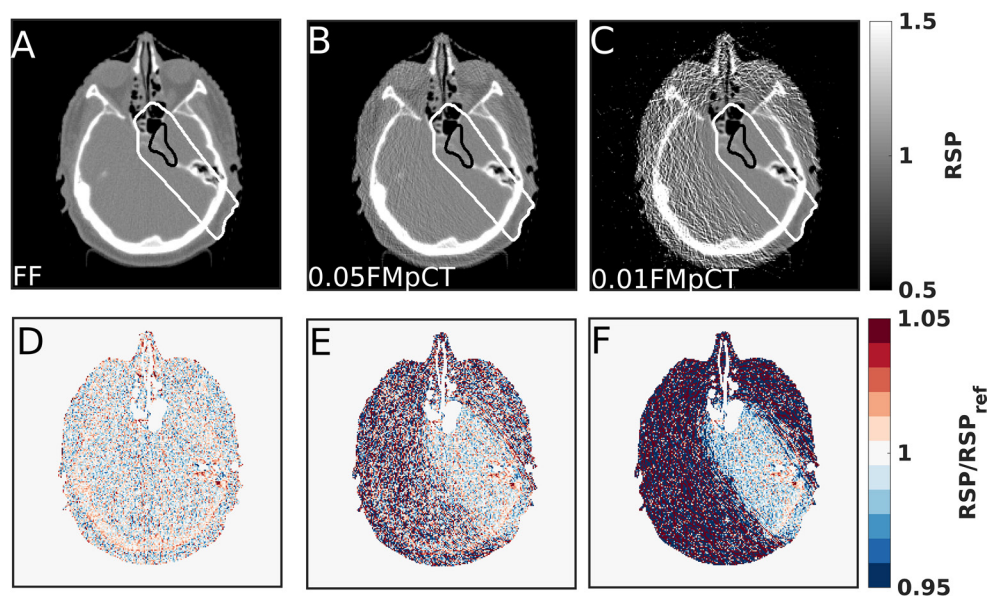


Figure 5. (A) FF pCT image for Pat1. FMpCT images with FMF of (B) 0.05 and (C) 0.01. (A)–(C) The PTV (black) and FMpCT ROI (white) are overlaid on the pCT images. (D)–(F) Corresponding relative RSP images.

noise and accuracy in the ROIs, indicated by the black circles, showed negligible difference from those of the FF image for FMF = 0.1 and 0.05. At FMF = 0.01, the mean value in the ROI deviated by -1.3% from the reference image (see table S1 in supplementary materials) (stacks.iop.org/PMB/62/6026/mmedia). The imaging integral physical dose was reduced from 2.3 mGy in the FF image to 0.7 mGy in the FMF = 0.1 FMpCT image (see figure S1 in supplementary material). Additionally, the results of the RSP noise and accuracy analysis did not vary as a function of the ROI location (see figure S2 in supplementary material).

3.2. SFUD and IMPT cases

Figure 5 shows the uniform FF as well as FMpCT with FMF = 0.05 and 0.01 for Pat1, where we observed better image quality in the FMpCT ROI used to cover the SFUD beam path than outside. For FMF = 0.05, the RSP/RSP_{ref} in the FMpCT image is similar in the ROI as the FF image, however for FMF = 0.01 slightly lower RSP values were observed. Figure 6 presents noise and accuracy as a function of the FMF for Pat1, where we observed that for $FMF < 0.025$ the noise increases more than expected from the statistical dependence on $(\text{number of protons})^{-1/2}$ and that the accuracy begins to degrade even with FMpCT.

Figure 7 shows the pCT images for Pat2, where similar image quality preservation as Pat1 was obtained from FMpCT. This can be appreciated in table 1 where the results of the RSP noise and accuracy in the ROIs are tabulated for both patients. The noise levels for Pat1 and Pat2 are comparable to those from the uniform cylinder (table S1) at FMF = 0.1 and FMF = 0.05. At FMF = 0.01, the patient images exhibited higher noise. For both Pat1 and Pat2 the FMF = 0.01 caused a slightly increased mean error of 0.6% and 0.5%, respectively, for the uniform fluence, and -0.7% and -0.4% , respectively, for the FMpCT (visible in figures 5(F) and 7(F), respectively), which is comparable to what was observed with the cylindrical phantom.

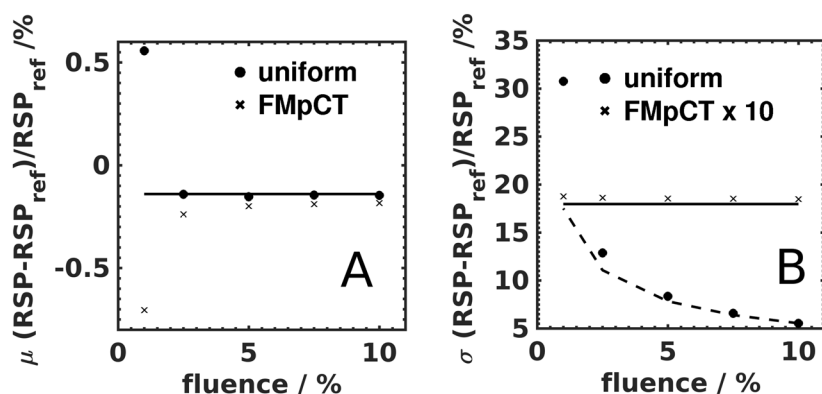


Figure 6. (A) Accuracy (mean, μ) of uniform and FMpCT images for various FMF (expressed as percentage of FF) in the ROI of Pat1. The horizontal solid line corresponds to the FF accuracy. (B) Noise (1 standard deviation, σ) of the same distributions. The FMpCT data are multiplied by 10. The horizontal solid line corresponds to the FF noise $\times 10$ and the dashed line to $\sigma_{10\%}(\text{fluence}/10\%)^{-1/2}$.

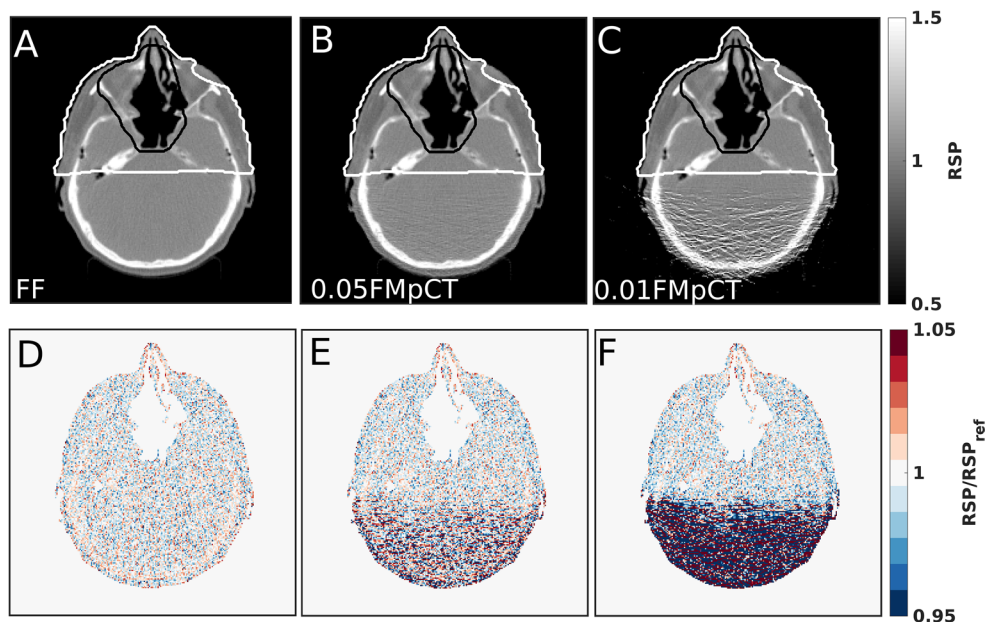


Figure 7. (A) FF pCT image for Pat2. FMpCT images with FMF of (B) 0.05 and (C) 0.01. (A)–(C) The lower dose PTV (black) and FMpCT ROI (white) are overlaid on the pCT images. (D)–(E) Corresponding relative RSP images.

In figure 8, the imaging dose distributions in the case of uniform FF and FMpCT illustrate the imaging dose reduction achieved for both the SFUD and IMPT cases considered in this study. Table 2 presents the integral doses in the whole image as well as outside the ROIs for both patients. For Pat1 with a small PTV, the integral dose reduction was up to 49% for the whole image and 56% outside the ROIs with FMF = 0.01. For Pat2, smaller integral dose savings were realized due to the larger PTV and higher number of beams with the same FMF,

Table 1. RSP noise (1 standard deviation) and accuracy (mean) results in ROIs for the SFUD (Pat1) and IMPT (Pat2) cases. The second column shows RSP noise values for uniform scans with different FMF. The third column reports noise levels with FMpCT. The fourth and fifth columns refer to the RSP mean reconstructed values in the ROIs for the same imaging configuration.

Pat1	$(RSP - RSP_{ref})/RSP_{ref} (\%)$		$(RSP - RSP_{ref})/RSP_{ref} (\%)$		
	Noise		Mean		
	Uniform	FMpCT	Uniform	FMpCT	
FF	1.8	—	-0.1	—	
0.1 · FF	5.5	1.8	-0.1	-0.2	
0.05 · FF	8.3	1.8	-0.2	-0.2	
0.01 · FF	30.1	1.9	0.6	-0.7	
Pat2	$(RSP - RSP_{ref})/RSP_{ref} (\%)$		$(RSP - RSP_{ref})/RSP_{ref} (\%)$		
Pat2	Noise		Mean		
	Uniform	FMpCT	Uniform	FMpCT	
	FF	1.4	—	-0.2	—
	0.1 · FF	4.2	1.5	-0.2	-0.2
	0.05 · FF	6.3	1.6	-0.2	-0.2
0.01 · FF	32.5	1.6	0.5	-0.4	

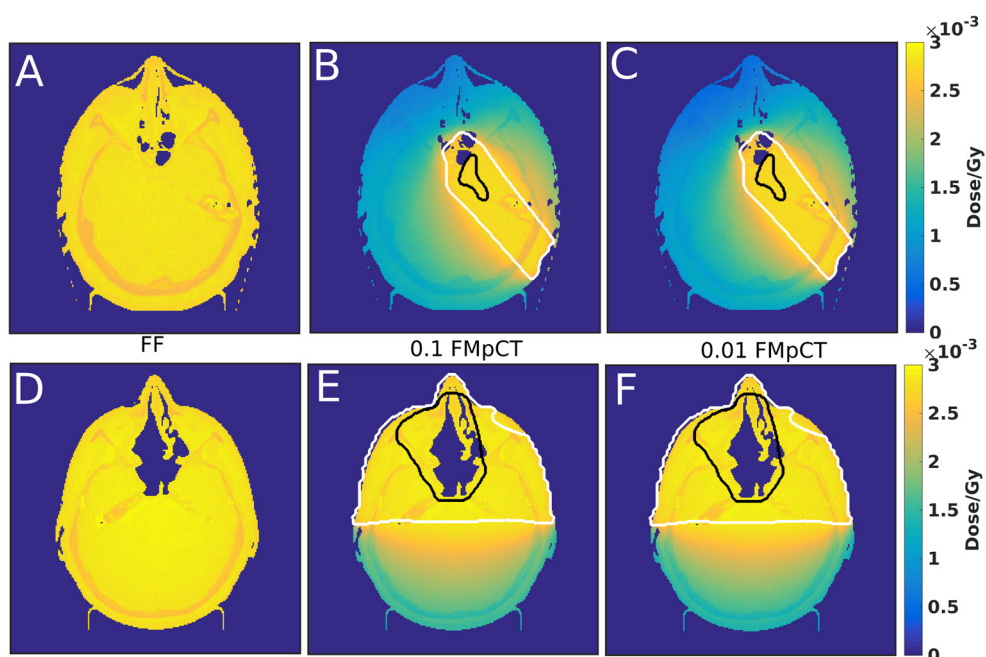


Figure 8. (top row) Pat1 imaging dose distributions on the (A) FF image, (B) 0.1 FMpCT and (C) the 0.01 FMpCT image. (bottom row) (D)–(F) Same for Pat2.

with a reduction of up to 22% for the whole image and 37% outside the ROI. Interestingly, changing FMF from 0.1 to 0.01 had an effect of less than 5% on integral dose reduction for both cases.

Table 2. Imaging dose in the complete volume and outside the ROI for both patients.

Pat1	Integral dose (mGy)		Integral dose reduction $1 - \text{FMF} \cdot \text{FMpCT}/\text{FF}$	
	Whole image	Outside ROI	Whole image	Outside ROI
FF	2.57	2.56	—	—
0.1 · FMpCT	1.42	1.25	0.45	0.51
0.05 · FMpCT	1.35	1.18	0.47	0.54
0.01 · FMpCT	1.30	1.12	0.49	0.56
<hr/>				
Pat2				
FF	2.67	2.65	—	—
0.1 · FMpCT	2.13	1.76	0.20	0.34
0.05 · FMpCT	2.10	1.71	0.21	0.35
0.01 · FMpCT	2.08	1.67	0.22	0.37

The dose calculation accuracy for the SFUD and IMPT treatment plans is presented in figure 9 for $\text{FMF} = 0.01$. We observed that the dose distributions calculated on the FMpCT images agreed with those calculated on the reference RSP_{ref} image in terms of isodose levels and DVH curves. This was not the case for the uniform $\text{FMF} = 0.01$ image where dose calculation accuracy was degraded as shown on the DVH of figure 9. This was confirmed by the (2%, 2 mm) gamma index analysis presented in table 3. For $\text{FMF} = 0.05$, the DVH curves of uniform fluence and FMpCT were identical to the reference.

For the SFUD beam of Pat1, 96% of BEV dose profiles had range differences lower than 2 mm versus RSP_{ref} for $\text{FMF} = 0.01$ FMpCT, while with the uniform $\text{FMF} = 0.01$ pCT only 1% of profiles passed this test. The $\text{FMF} = 0.05$ FMpCT results compared to RSP_{ref} show limited range agreement improvement compared to reduced uniform fluence (90% versus 87% respectively). When comparing the FMpCT and reduced uniform fluence to the FF case a clear improvement was seen (99% versus 88% respectively). This result indicates that at this modulation level ($\text{FMF} = 0.05$), FMpCT retains better agreement with the FF image than the uniform $\text{FMF} = 0.05$ image. The worst pass rate for FMpCT was 66% of profiles with range differences of less than 1 mm when comparing $\text{FMF} = 0.01$ and RSP_{ref} . However when comparing the same FMpCT image to the FF image, the pass rate rose to 97%, indicating that the lower pass rate was caused by a combination of sub-mm FMpCT errors compared to FF, and sub-mm systematic FF errors compared to RSP_{ref} . The range analysis was found to be sensitive to the air cavity abutting the PTV (see figure 5(A)) which caused small range shifts in tissue to be expanded in air. We verified that the 93% pass rate of FF pCT versus RSP_{ref} was caused by beam profiles ending in the air cavity.

The results of applying FMpCT to broad beam pCT scans of the pediatric head phantom are shown in figure 10 for the three FMF investigated. We observed a similar trend of reduced accuracy at lower FMF, however this happened at higher FMF for the experimental data. The noise and accuracy are reported in figure 11, where we observed that FMpCT with FMF below 0.3 showed accuracy degradation larger than 1% as well as increasing noise in the ROI. In Giacometti *et al* (2017), the theoretical RSP for the brain material of the pediatric phantom is reported as 1.047; the mean value in the ROI of the FF pCT image was 1.04 ± 0.03 , i.e. -0.7% lower than the reference. Please note that the theoretical RSP may differ from that measured in a proton beam due to uncertainties on the material composition.

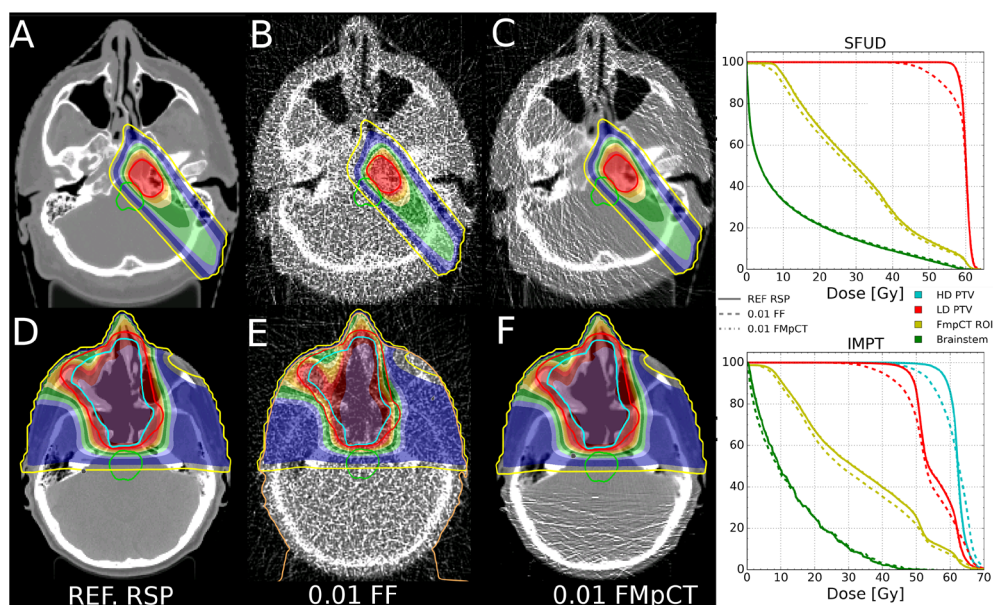


Figure 9. (top row) Pat 1 SFUD dose calculation on the (A) SPR_{ref} image, (B) $0.01 \cdot FF$ image and (C) the $0.01 \cdot FMpCT$ image. (bottom row) Pat 2 IMPT dose calculation on the (D) SPR_{ref} image, (E) $0.01 \cdot FF$ image and (F) the $0.01 \cdot FMpCT$ image. The corresponding DVHs are shown on the right.

Table 3. SFUD BEV range difference for Pat1. The percentage of profiles with range differences (RDs) below 1 mm and 2 mm are shown. RD are reported using the dose distribution calculated on the RSP_{ref} image and the FF image as reference. For Pat1 and Pat2, the percentage of voxels passing the (2%, 2 mm) gamma evaluation is also reported.

Pat1	RD < 1 mm (%)		RD < 2 mm (%)		Pat1		Pat2	
	Uniform	FMpCT	Uniform	FMpCT	Gamma (2%, 2 mm)			
					Uniform	FMpCT	Uniform	FMpCT
FF – RSP_{ref}	93	—	99	—	99	—	99	—
$0.05 \cdot FF - RSP_{ref}$	87	90	99	99	99	99	99	99
$0.01 \cdot FF - RSP_{ref}$	0	66	1	96	90	98	59	99
$0.05 \cdot FF - FF$	88	99	99	99	—	—	—	—
$0.01 \cdot FF - FF$	0	97	0	99	—	—	—	—

4. Discussion

The results shown in figure 4 qualitatively support our hypothesis that FMpCT image reconstruction is feasible when employing the binary fluence modulation scheme presented in figure 1. For the three levels of fluence reduction outside ROI2, two distinct image quality levels were seen in each image. The image quality metrics reported in table S1 show that in the case of homogeneous fluence, the noise was approximately inversely proportional to the square root of the proton fluence, while FMpCT reconstruction preserved image quality (both standard deviation and mean value) down to 5% of the FF. However for $FMF = 0.01$, we observed a break from the $(\text{number of protons})^{-1/2}$ dependence of the noise as well as

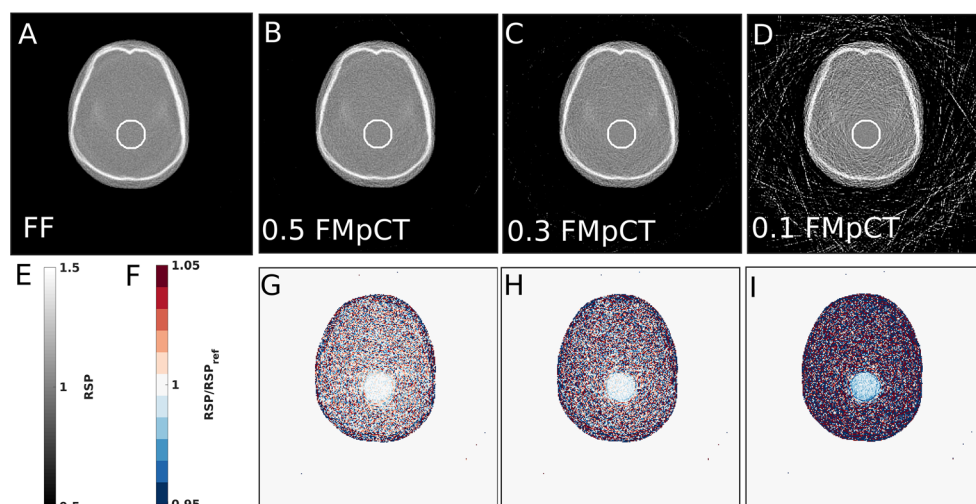


Figure 10. (A) FF pCT and (B) 0.5 (C) 0.3 and (D) 0.1 FMpCT images for the pediatric head phantom and (E) their colorbar. (A)–(D) The FMpCT ROI (white) used for modulation and analysis is overlaid on the pCT images. (G)–(I) Corresponding relative RSP images and (F) their colorbar. In this case RSP_{ref} is the FF image.

a -1.3% shift of the mean values in the ROI, indicating a limit to the modulation level feasible with FMpCT. A similar effect was observed for the patient and experimental data. Our initial investigations on the root of this error indicate that one cause of the problem is the inaccurate estimate of the 3 standard deviations cuts from a small number of protons which then fail to eliminate some protons that have encountered nuclear interactions.

The higher threshold where this happens for the experimental data compared to the simulated data may be explained by the use of ideal detectors in the simulations. A follow up study making use of the simulation framework presented in Giacometti *et al* (2017) would help clarify this.

Given the nature of the FMpCT approach, the dose reduction was not uniform throughout the images (see figures 8 and S1) but was the highest at the largest distance to the ROI. The imaging dose reduction outside the ROI might be particularly important for proton therapy imaging since the non-target treatment dose is usually lower than for conventional x-ray based radiotherapy, potentially reducing the induction of secondary cancers (Miralbell *et al* 2002, Paganetti *et al* 2012, Fuji *et al* 2013). Avoiding additional non-target dose from image guidance is thus warranted.

For the homogeneous fluence imaging case, the imaging dose was uniform partly due to the fact that the Bragg peak falls outside the object, which means that the protons traversing it produce a relatively flat dose distribution along their path. This situation is very different from kV x-ray CT where higher dose is observed at the object's edge due to the shape of the depth dose profile of photon beams (Bartolac *et al* 2011, Arbor *et al* 2015).

The dose levels reported in this study for the virtual phantoms are based on MC simulation of ideal detectors. Effect such as pileup would contribute to a higher dose compared to our ideal simulation at equivalent image quality. However, the magnitude of the relative dose reduction should not be greatly influenced by the efficiency of real detectors. The lowest possible FMF where image quality is maintained would however probably be higher for realistic detectors.

The experimental list-mode data made use of 90 projections with $12\,000$ protons cm^{-2} at the center of a projection while the simulated list-mode data used 360 projections with 9600

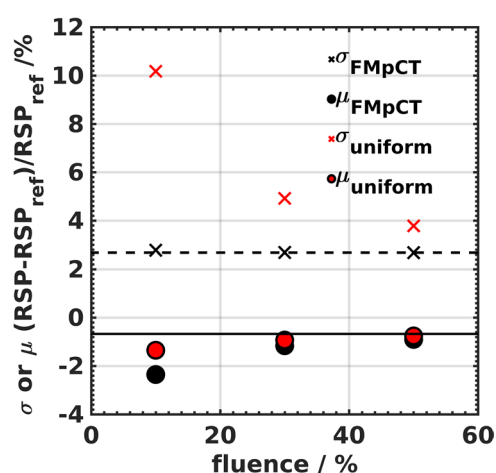


Figure 11. Accuracy (mean, μ) and noise (1 standard deviation, σ) of FMpCT images (black data points) and uniform images (red data points) for various FMF (expressed as percentage of FF) in the ROI of the pediatric head phantom. The horizontal dashed (solid) line corresponds to the FF noise (accuracy).

protons cm^{-2} (3.2 times more protons). For both experimental and simulated data, one should keep in mind that the list-mode data used for image reconstruction are not equivalent to the proton fluence incident on the first tracker module since they consist of protons with entrance and exit coordinates. In the simulated data this excludes mostly protons which underwent nuclear interactions. For the experimental data, various additional detector effects exclude protons from the list-mode data, making estimation of the dose for experimental scans based on simulated scan doses a rough approximation (about 1 mGy). At the time of writing, no direct dose estimation was available for the experimental data. A separate project involving a dosimetric phantom and appropriate detectors is underway by some of the co-authors.

In this first attempt at FMpCT, we made use of a simple binary fluence modulation scheme; a more sophisticated fluence optimization approach may yield different spatial dose distributions for equivalent image quality and deserves further investigation. The conformity of the imaging dose to the ROI may be improved by employing continuously varying fluence modulation profiles and an optimization procedure instead of the binary scheme employed in this proof of principle study. The reason our simple modulation scheme yielded rather acceptable results is attributed to the low attenuation of protons. Indeed, the attenuation of protons traversing 20 cm of water is around 19% for 200 MeV protons and 18% for 300 MeV protons (Quinones *et al* 2016). Additionally, the inelastic proton cross section is almost independent of the proton energy in the energy range 100–300 MeV. Compared to x-rays, for which 97% of 80 keV photons would be attenuated after 20 cm of water, the calculation of the modulation pattern necessary to obtain the desired image quality is thus more forgiving for FMpCT than FFMCT. Proton dose deposition in the 200–300 MeV range also has a lower material dependency (mass stopping power ratio) than photons in the diagnostic energy range (mass energy absorption coefficient ratio), yielding more homogeneous imaging dose distributions.

We have found very little published literature on the impact of CT noise on proton therapy dose calculation, with one report stating that discontinuities in the CT number to RSP lookup table might introduce range shifts in the presence of stochastic noise (Brousmiche *et al* 2015). This is not the case for proton CT which has a linear lookup table (Arbor *et al* 2015). High levels of noise on CT images can additionally cause a spread of the range at which protons

stop, the width of which (4 standard deviations) can reach a few percent of the range at 5.0% CT number noise (Chvetsov and Paige 2010).

This study was based on the use of 1 cm (FWHM) proton PBs. This value is a realistic estimation of the PB size available at clinical facilities. The current prototype scanner has been used with PB of minimum size of 4 cm (FWHM). Due to pileup in the tracker, the maximum counting rate for a PB size of 1 cm is approximately 200 kHz. For Pat1, this would mean about 9 s per projection at full fluence, resulting into a total scan time of 13.5 min for 90 projections or 54 min for 360 projections. For realistic scan duration, the electronics of the Phase II prototype would have to be modified. The current electronics were designed according to a conservative approach and assuming only scattered proton beams. Therefore, an upgrade to faster electronics is not considered a technical obstacle and significantly faster electronics have been already developed and used in other pCT prototypes (Taylor *et al* 2016). To achieve a pCT scan with 1 cm PBs, without any hardware modification to the scanner, a reduction of the beam intensity will be required. It remains to be investigated whether that can allow for a dynamic range necessary for FMpCT studies. Alternatively, a more sophisticated fluence modulation technique than the binary intersection pattern could compensate for the larger PB size.

Although initially explored in the context of pCT with advanced detectors tracking individual protons, the method could also be applicable to integrating detectors such as range telescopes (Krah *et al* 2015, Farace *et al* 2016) or using 2D detectors (Lee *et al* 2015, Tanaka *et al* 2016) being also under development. Moreover, the same concept could be extended to imaging with other ions such as ^4He and ^{12}C (Shinoda *et al* 2006, Hansen *et al* 2014, Rinaldi *et al* 2014).

The concept of fluence modulation can be supplemented by energy modulation as well, as pCT imaging dose and noise levels are energy dependent, and we intend to investigate it as a continuation of the current study.

5. Conclusion

In this work, we have applied the concept of fluence field modulation to proton CT, inspired by earlier work applied to x-ray CT. Using Monte Carlo simulations of an ideal proton CT scanner, we have confirmed that image quality could be varied across the proton CT image by modulating the proton fluence in a binary fashion. Our approach was successful for both homogeneous and anthropomorphic virtual phantoms, potentially allowing clinical imaging dose reductions ranging from 37% to 56% outside the treatment area, while preserving full fluence image quality inside regions of interest. We additionally virtually implemented the method on broad beam proton CT experimental data and showed that fluence modulated proton CT should be realizable if proton PB intensity and detector count rates can be adjusted to achieve the desired modulation levels.

Acknowledgments

This work was supported by the German Research Foundation (DFG) Cluster of Excellence Munich-Centre for Advanced Photonics (MAP), by the Bavaria-California Technology Center (BaCaTeC) and by the Bavaria-France Cooperation Centre (BFHZ). Dr U Ganswindt from the Department of Radiation Oncology of the LMU is acknowledged for sharing and delineating the patient CT scan used in this study. The authors thank Erik Traneus from RaySearch Laboratories for his support on the RayStation TPS. Advice on PBS treatment planning from Martin Hillbrand is gratefully acknowledged.

References

- Agostinelli S *et al* 2003 Geant4—a simulation toolkit *Nucl. Instrum. Methods A* **506** 250–303
- Arbor N *et al* 2015 Monte Carlo comparison of x-ray and proton CT for range calculations of proton therapy beams *Phys. Med. Biol.* **60** 7585–99
- Bartolac S *et al* 2011 Fluence field optimization for noise and dose objectives in CT *Med. Phys.* **38** S2
- Bartolac S and Jaffray D 2013 Compensator models for fluence field modulated computed tomography *Med. Phys.* **40** 121909
- Brousic S *et al* 2015 TH-CD-BRA-04: assessing how stochastic CT noise can lead to systematic proton range errors *Med. Phys.* **42** 3726
- Chvetsov A V and Paige S L 2010 The influence of CT image noise on proton range calculation in radiotherapy planning *Phys. Med. Biol.* **55** N141–9
- Cormack A M 1963 Representation of a function by its line integrals with some radiological applications *J. Appl. Phys.* **34** 2722
- Farace P *et al* 2016 Pencil beam proton radiography using a multilayer ionization chamber *Phys. Med. Biol.* **61** 4078–87
- Fuji H *et al* 2013 Assessment of organ dose reduction and secondary cancer risk associated with the use of proton beam therapy and intensity modulated radiation therapy in treatment of neuroblastomas *Radiat. Oncol.* **8** 255
- Giacometti V *et al* 2017 Software platform for simulation of a prototype proton CT scanner *Med. Phys.* **44** 1002–16
- Graham S A *et al* 2007a Compensators for dose and scatter management in cone-beam computed tomography *Med. Phys.* **34** 2691–703
- Graham S A, Siewerdsen J H and Jaffray D A 2007b Intensity-modulated fluence patterns for task-specific imaging in cone-beam CT *Proc. SPIE* **6510** 651003
- Hansen D C *et al* 2014 The image quality of ion computed tomography at clinical imaging dose levels *Med. Phys.* **41** 111908
- Hansen D C *et al* 2015 A simulation study on proton computed tomography (CT) stopping power accuracy using dual energy CT scans as benchmark *Acta Oncol.* **54** 1638–42
- Hansen D C *et al* 2016 Fast reconstruction of low dose proton CT by sinogram interpolation *Phys. Med. Biol.* **61** 5868–82
- Hudobivnik N *et al* 2016 Comparison of proton therapy treatment planning for head tumors with a pencil beam algorithm on dual and single energy CT images *Med. Phys.* **43** 495
- Huesman R H, Rosenfeld A and Solmitz F 1975 Comparison of heavy charged particles and x-rays for axial tomographic scanning *Technical Report* Technical Information Center US Department of Energy (<https://doi.org/10.2172/4146950>)
- Hünemohr N *et al* 2013 Ion range estimation by using dual energy computed tomography *Z. Med. Phys.* **23** 300–13
- Hünemohr N *et al* 2014 Experimental verification of ion stopping power prediction from dual energy CT data in tissue surrogates *Phys. Med. Biol.* **59** 83–96
- Hurley R F *et al* 2012 Water-equivalent path length calibration of a prototype proton CT scanner *Med. Phys.* **39** 2438–46
- Johnson R P *et al* 2016 A fast experimental scanner for proton CT: technical performance and first experience with phantom scans *IEEE Trans. Nucl. Sci.* **63** 52–60
- Kalender W A *et al* 2008 Technical approaches to the optimisation of CT *Phys. Med.* **24** 71–9
- Krah N *et al* 2015 An advanced image processing method to improve the spatial resolution of ion radiographies *Phys. Med. Biol.* **60** 8525–47
- Kurz C *et al* 2015 Comparing cone-beam CT intensity correction methods for dose recalculation in adaptive intensity-modulated photon and proton therapy for head and neck cancer *Acta Oncol.* **54** 1651–7
- Landry G *et al* 2015a Phantom based evaluation of CT to CBCT image registration for proton therapy dose recalculation *Phys. Med. Biol.* **60** 595
- Landry G *et al* 2015b Investigating CT to CBCT image registration for head and neck proton therapy as a tool for daily dose recalculation *Med. Phys.* **42** 1354–66
- Lee J *et al* 2015 Sparse-view proton computed tomography using modulated proton beams *Med. Phys.* **42** 1129–37
- Mail N *et al* 2009 The influence of bowtie filtration on cone-beam CT image quality *Med. Phys.* **36** 22–32

- McCollough C H *et al* 2006 CT dose reduction and dose management tools: overview of available options *Radiographics* **26** 503–12
- Miralbell R *et al* 2002 Potential reduction of the incidence of radiation-induced second cancers by using proton beams in the treatment of pediatric tumors *Int. J. Radiat. Oncol. Biol. Phys.* **54** 824–9
- Mohler C *et al* 2016 Range prediction for tissue mixtures based on dual-energy CT *Phys. Med. Biol.* **61** N268–75
- Mulkens T H *et al* 2005 Use of an automatic exposure control mechanism for dose optimization in multi-detector row CT examinations: clinical evaluation *Radiology* **237** 213–23
- Murphy M J *et al* 2007 The management of imaging dose during image-guided radiotherapy: report of the AAPM Task Group 75 *Med. Phys.* **34** 4041–63
- Paganetti H 2012 Range uncertainties in proton therapy and the role of Monte Carlo simulations *Phys. Med. Biol.* **57** R99–117
- Paganetti H *et al* 2012 Assessment of radiation-induced second cancer risks in proton therapy and IMRT for organs inside the primary radiation field *Phys. Med. Biol.* **57** 6047
- Park Y K *et al* 2015 Proton dose calculation on scatter-corrected CBCT image: feasibility study for adaptive proton therapy *Med. Phys.* **42** 4449–59
- Penfold S N *et al* 2009 A more accurate reconstruction system matrix for quantitative proton computed tomography *Med. Phys.* **36** 4511–8
- Penfold S N *et al* 2010 Total variation superiorization schemes in proton computed tomography image reconstruction *Med. Phys.* **37** 5887–95
- Quinones C T *et al* 2016 Filtered back-projection reconstruction for attenuation proton CT along most likely paths *Phys. Med. Biol.* **61** 3258–78
- Rinaldi I *et al* 2014 Experimental investigations on carbon ion scanning radiography using a range telescope *Phys. Med. Biol.* **59** 3041–57
- Rit S *et al* 2013 Filtered backprojection proton CT reconstruction along most likely paths *Med. Phys.* **40** 031103
- Sadrozinski H F W *et al* 2016 Operation of the preclinical head scanner for proton CT *Nucl. Instrum. Methods Phys. Res. A* **831** 394–9
- Schmid S *et al* 2015 Monte Carlo study on the sensitivity of prompt gamma imaging to proton range variations due to interfractional changes in prostate cancer patients *Phys. Med. Biol.* **60** 9329–47
- Schneider W *et al* 2000 Correlation between CT numbers and tissue parameters needed for Monte Carlo simulations of clinical dose distributions *Phys. Med. Biol.* **45** 459–78
- Schulte R W *et al* 2005 Density resolution of proton computed tomography *Med. Phys.* **32** 1035–46
- Schulte R W *et al* 2008 A maximum likelihood proton path formalism for application in proton computed tomography *Med. Phys.* **35** 4849–56
- Shinoda H *et al* 2006 Application of heavy-ion CT *Phys. Med. Biol.* **51** 4073–81
- Stayman J W, Mathews A, Zbijewski W, Gang G, Siewerdsen J, Kawamoto S, Blevis I and Levinson R 2016 Fluence-field modulated x-ray CT using multiple aperture devices *Proc. SPIE* **9783** 97830X
- Szczykutowicz T P and Mistretta C A 2013a Design of a digital beam attenuation system for computed tomography: part I. System design and simulation framework *Med. Phys.* **40** 021905
- Szczykutowicz T P and Mistretta C A 2013b Design of a digital beam attenuation system for computed tomography. Part II. Performance study and initial results *Med. Phys.* **40** 021906
- Szczykutowicz T P and Mistretta C A 2014 Experimental realization of fluence field modulated CT using digital beam attenuation *Phys. Med. Biol.* **59** 1305–26
- Szczykutowicz T P *et al* 2015 Realization of fluence field modulated CT on a clinical TomoTherapy megavoltage CT system *Phys. Med. Biol.* **60** 7245–57
- Tanaka S *et al* 2016 Development of proton CT imaging system using plastic scintillator and CCD camera *Phys. Med. Biol.* **61** 4156–67
- Taylor J T *et al* 2016 An experimental demonstration of a new type of proton computed tomography using a novel silicon tracking detector *Med. Phys.* **43** 6129
- Veiga C *et al* 2015 Cone-beam computed tomography and deformable registration-based ‘dose of the day’ calculations for adaptive proton therapy *Int. J. Part. Ther.* **2** 404–14
- Veiga C *et al* 2016 First clinical investigation of cone beam computed tomography and deformable registration for adaptive proton therapy for lung cancer *Int. J. Radiat. Oncol. Biol. Phys.* **95** 549–59
- Yang M *et al* 2012 Comprehensive analysis of proton range uncertainties related to patient stopping-power-ratio estimation using the stoichiometric calibration *Phys. Med. Biol.* **57** 4095–115